



**HAL**  
open science

## **Beam shaping to enhance zero group velocity Lamb mode generation in a composite plate and nondestructive testing application**

Frédéric Faëse, Samuel Raetz, Nikolay Chigarev, Charfeddine Mechri, James Blondeau, Benjamin Campagne, Vitali Goussev, Vincent Tournat

### ► **To cite this version:**

Frédéric Faëse, Samuel Raetz, Nikolay Chigarev, Charfeddine Mechri, James Blondeau, et al.. Beam shaping to enhance zero group velocity Lamb mode generation in a composite plate and nondestructive testing application. *NDT & E International*, 2017, 85, pp.13 - 19. <10.1016/j.ndteint.2016.09.003>. <hal-01889431v2>

**HAL Id: hal-01889431**

**<https://univ-lemans.hal.science/hal-01889431v2>**

Submitted on 27 Apr 2019

**HAL** is a multi-disciplinary open access archive for the deposit and dissemination of scientific research documents, whether they are published or not. The documents may come from teaching and research institutions in France or abroad, or from public or private research centers.

L'archive ouverte pluridisciplinaire **HAL**, est destinée au dépôt et à la diffusion de documents scientifiques de niveau recherche, publiés ou non, émanant des établissements d'enseignement et de recherche français ou étrangers, des laboratoires publics ou privés.



HAL Authorization

1 Beam shaping to enhance zero group velocity Lamb  
2 mode generation in a composite plate and  
3 nondestructive testing application

4 Frédéric Faëse<sup>a,b</sup>, Samuel Raetz<sup>b,\*</sup>, Nikolay Chigarev<sup>b</sup>, Charfeddine Mechri<sup>b</sup>,  
5 James Blondeau<sup>b</sup>, Benjamin Campagne<sup>c</sup>, Vitalyi E. Gusev<sup>b</sup>, Vincent  
6 Tournat<sup>b,1,\*\*</sup>

7 <sup>a</sup>*IRT Jules Verne, Chemin du Chaffault, 44340 BOUGUENNAIS - France*

8 <sup>b</sup>*Université du Maine, CNRS, LAUM UMR 6613, Av. O. Messiaen, 72085 LE MANS  
9 Cedex 9 - France*

10 <sup>c</sup>*Airbus Group Innovations, Chemin du Chaffault, 44340 BOUGUENNAIS - France*

---

11 **Abstract**

Zero group velocity (ZGV) Lamb modes have already shown their potential in nondestructive testing applications as they are sensitive to the sample structural characteristics. In this paper, we first consider an aluminum sample to validate a method based on the beam shaping of the generation laser. This method is proven to enhance ZGV Lamb modes in aluminum, and then advantageously applied to a composite material plate. Finally, based on the proposed method, scanning the sample over healthy and flawed zones demonstrates the ability to detect subsurface flaws.

12 *Keywords:* Laser ultrasonics, Composite materials, Zero Group Velocity  
13 Lamb modes, NDT

---

\*Corresponding author

\*\*Principal corresponding author

*Email addresses:* [samuel.raetz@univ-lemans.fr](mailto:samuel.raetz@univ-lemans.fr) (Samuel Raetz),  
[vincent.tournat@univ-lemans.fr](mailto:vincent.tournat@univ-lemans.fr) (Vincent Tournat)

<sup>1</sup>Currently at: John A. Paulson School of Engineering and Applied Science, Harvard University, Cambridge, MA 02138, USA

*Preprint submitted to NDT&E International*

*August 4, 2016*

## 14 1. Introduction

15 Laser ultrasonics is a more and more widespread nondestructive testing  
16 method as it shows specific advantages compared to conventional ultrasonic  
17 methods based on transducers or EMATs. Particularly, it has a high spatial  
18 resolution, a large bandwidth, and it is non-contact [1]. Thanks to these fea-  
19 tures, laser ultrasonic techniques allow characterizing the mechanical prop-  
20 erties and/or evaluating the structural health of materials, even where the  
21 tested samples present complex geometry and/or are subjected to extreme  
22 conditions such as high temperatures [2]. Up to now, applications of laser  
23 ultrasonic methods have already proved their potential in nondestructive  
24 testing of composite materials. They have been implemented successfully to  
25 detect delaminations with a propagative Lamb waves analysis [3] or by laser  
26 tapping [4]. They have also the ability to detect fiber breakage or matrix  
27 cracking via the scanning laser source technique [5] or even porosity thanks  
28 to an ultrasonic spectroscopy method [6].

29 Guided waves have been used in composite samples testing and evalua-  
30 tion because of their ability to detect a defect at a long propagation distance  
31 from the acoustic source position. Yet, the defect position is hard to pre-  
32 cisely estimate at a single interface at any position through the laminate [3].  
33 As well, a lateral position estimation needs methods with a transducer raster  
34 scan like the SAFT method [7] or transducer arrays like the topological imag-  
35 ing technique [8]. For ten years, some specific non-propagative Lamb modes  
36 called zero group velocity (ZGV) Lamb modes have been studied and already  
37 applied to defect detection. Considering a dispersion curve representing the  
38 angular frequency  $\omega$  as a function of the wave number  $k$ , these specific modes

39 are located in the points of a non-zero wave number  $k$  where the slope of this  
40 curve is horizontal, i.e.  $d\omega/dk = 0$ . Characterized by a high quality factor,  
41 these modes are used for instance to measure thickness variations due to  
42 corrosion, to detect disbonding or to determine elastic constants [9, 10]. A  
43 method based on the ZGV Lamb modes offers the advantages of being local  
44 and having a spatial resolution of the order of the plate thickness [10]. One  
45 objective of this article is to report on the effect of a flaw in a composite  
46 plate on ZGV Lamb modes.

47 The challenges to address when generating ZGV Lamb modes in com-  
48 posite plates are numerous. Firstly, the composite plates usually have a low  
49 damage threshold. For instance, the sample used in this paper showed fiber  
50 whitening at about  $5 \text{ MW.cm}^{-2}$  with a 1064 nm-wavelength laser, whereas  
51 the threshold for aluminum in the same experimental conditions is about 50  
52  $\text{MW.cm}^{-2}$  [11]. Secondly, as composite surfaces are matt and diffusive for  
53 light, ultrasonic waves are hardly detectable using non-contact optical tech-  
54 niques. Thirdly, quality factors of ZGV Lamb modes are strongly reduced  
55 because of the resin viscoelasticity leading to a strong sound attenuation in  
56 composite plates. Note that ZGV Lamb modes could even not exist, regard-  
57 ing the anisotropic mechanical properties of the material; nevertheless, this  
58 is out of the focus of this paper.

59 In this work, elastic waves are generated in an aluminum plate or a com-  
60 posite plate by a pulsed laser and detected using an interferometer. By  
61 varying the focusing of the pump laser beam, it is possible to favor the  
62 generation of either the propagating modes or the ZGV modes in the plate.  
63 Especially, considering a circular laser spot as the thermoelastic source, ZGV

64 Lamb modes are efficiently excited when the spot radius is about the plate  
65 thickness [12]. It is first shown that ZGV Lamb modes can be enhanced  
66 or reduced in an aluminum plate thanks to a specific beam shaping of the  
67 generation laser [13–17]. Then, the same method is advantageously applied  
68 to the healthy zone of a composite plate. Finally, a damaged region of the  
69 same composite plate is considered and the influences of the flaw on the  
70 ZGV Lamb modes are analyzed. Before going into details, the mechanical  
71 properties of the tested sample and the experimental setups are introduced.

## 72 **2. Mechanical properties of the tested sample and experimental** 73 **setups**

74 This section is devoted to the analysis of the influence of flaws on ZGV  
75 Lamb modes in a plate made of composite material. As the setup is based  
76 on a beam-shaping mask to selectively generate a specific ZGV mode, it is  
77 important to know the mechanical properties of the tested material in order  
78 to design the beam-shaping mask. We will show that the optimal geometrical  
79 properties of the beam-shaping mask for a particular ZGV mode generation  
80 depend on the ZGV wavelength in the sample. In the framework of indus-  
81 trial nondestructive testing (NDT), mechanical properties of the composite  
82 materials are already well characterized. Hence, the wavelengths of the ZGV  
83 modes that can be generated in the sample are known. Here the mechan-  
84 ical properties of the composite sample were first characterized in order to  
85 determine an interesting ZGV mode and then to make the appropriate beam-  
86 shaping mask.

87 In order to predict the dispersion curve of the composite plate, both the  
88 density and the elastic constants have to be determined. First, the volu-

89 metric mass density of the composite sample has been estimated thanks to  
 90 Archimedes principle to be  $\rho_{comp} \approx 1540 \text{ kg.m}^{-3}$ . Second, the elastic con-  
 91 stants have been determined thanks to a method explained in Refs. [18]  
 92 and [19]. Based on appropriate A-scans, plane wavefronts are synthesized  
 93 by summing the signals with suitable delays. By changing the synthesized  
 94 propagation angle, quasi-longitudinal and quasi-transversal time of flights are  
 95 semi-automatically recorded. Finally, the theoretical slowness curve that fits  
 96 the experimental one is determined, thanks to a minimization method. This  
 97 leads to the following estimation of the elastic constants:  $C_{11} = 13.4 \text{ GPa}$ ,  
 98  $C_{12} = 3.00 \text{ GPa}$ ,  $C_{22} = 21.36 \text{ GPa}$ , and  $C_{55} = 3.64 \text{ GPa}$ . Note that these  
 99 constants have been obtained by assuming that the composite plate is trans-  
 100 versely isotropic relative to an axis normal to the surface. **The composite**  
 101 **plate is a carbon fiber-epoxy composite, composed of 10 plies of 300  $\mu\text{m}$ -thick**  
 102 **each, oriented as [45/0/0/45/0/45/0/45/0/45]. Thanks to the SAFE method,**  
 103 **the composite plate structure was confirmed to be transversely isotropic. Fi-**  
 104 **nally, from the measured plate thickness,  $d_{comp} \approx 3.2 \text{ mm}$ , the dispersion**  
 105 **curves have been calculated and are displayed in Fig. 1. As one could find in**  
 106 **literature [20, 21], ZGV Lamb mode can occur in anisotropic material and**  
 107 **the wavelength of the first ZGV Lamb mode in our composite plate (cf. ver-**  
 108 **tical arrow in Fig. 1 is here estimated with a precision that is sufficient for**  
 109 **the method we propose:  $\lambda_{ZGV}^{comp} \approx 15.3 \text{ mm}$ .**

110 Due to the low damage threshold of composite materials, the choice has  
 111 been done to experimentally use an extended line source instead of a circular  
 112 spot, in order to lower the source power density on the sample while keeping  
 113 sufficiently large displacement amplitude. Theoretically, using an infinitely

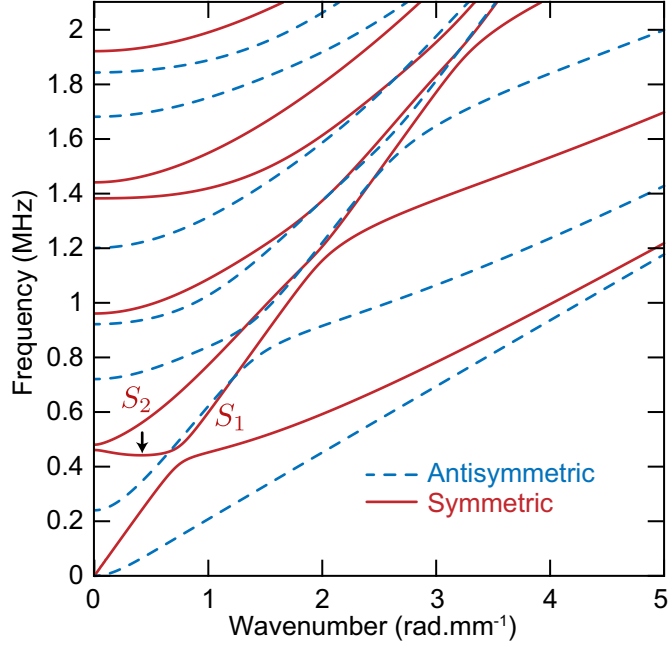


Figure 1: (color online) Dispersion curves of the symmetric (solid line) and antisymmetric (dashed line) Lamb modes calculated in a 3.2-mm-thick composite plate. The first ZGV mode is shown by the vertical arrow and has a wavelength of  $\lambda_{ZGV}^{comp} \approx 15.3$  mm.

114 long and thin thermoelastic line source, the amplitude of the surface displace-  
 115 ment due to a ZGV Lamb mode as a function of the distance from the line  
 116 source is a pure cosine function, since it results from the interference of two  
 117 counter-propagative Lamb modes having the same wave number, i.e. of the  
 118 form  $e^{jk_{ZGV}x}$  and  $e^{-jk_{ZGV}x}$ . In the case of a finite line source, the amplitude  
 119 varies as an intermediate function between the pure cosine function and a  
 120 Bessel function [22], the latter standing for the theoretical spatial distribu-  
 121 tion of ZGV Lamb modes in the case of a point surface source [12]. In order  
 122 to selectively generate the first ZGV Lamb mode and to increase the total in-  
 123 cident laser power while keeping the power density constant, we propose here

124 to use multiple finite line sources using an appropriate beam-shaping mask.  
125 As illustrated in Fig. 2, using the beam-shaping mask allows the generation  
126 laser beam to be shaped with periodic slits whose spacing matches the ZGV  
127 wavelength, thereby producing a constructive interference of the ZGV Lamb  
128 modes generated by each line source. Note that the laser transient grating  
129 technique[13–15] is another efficient technique to selectively generate elastic  
130 guided waves with a given wavelength. The use of an optical mask instead of  
131 the laser transient grating technique has been mainly chosen for the reason of  
132 experimental simplicity. Achieving a transient laser grating with such large  
133 period would have indeed required the laser beams to be crossed with a really  
134 small angle (about  $2.10^{-3}$  deg), which was technically difficult to reach with  
135 a good precision.

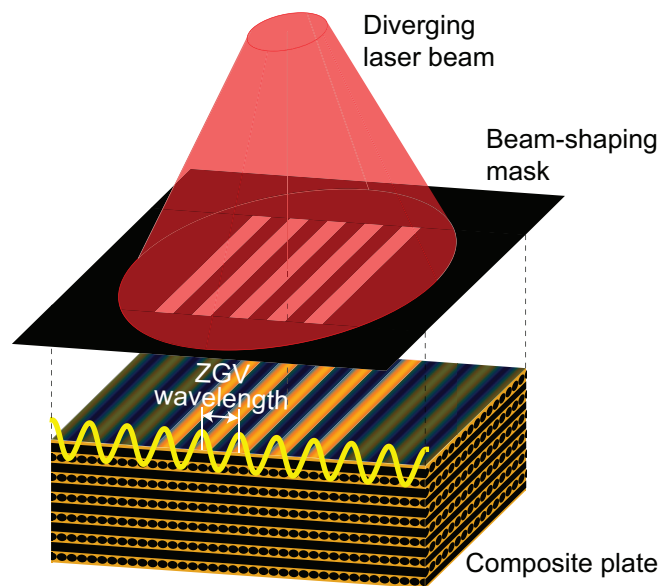


Figure 2: (color online) Illustration of the ZGV Lamb mode generation using a beam-shaping mask. The generation laser beam is shaped with periodic slits whose spacing matches the ZGV wavelength.

136 In order to analyze the ZGV Lamb mode generation using a shaped laser  
137 beam, **the experimental setup shown in Fig. 3 has been implemented.** The  
138 generation laser is an Nd:YAG laser (Spitlight Compact 400, InnoLas Laser  
139 GmbH, Germany) emitting 10 ns pulses at 1064 nm. The pulse energy is  
140 limited to a few tens of mJ in order to remain below the damage threshold  
141 and to avoid fiber whitening. This limitation of the laser energy is performed  
142 using two polarizing beam splitters (PBS) and a half-wave plate ( $\lambda/2$ ) as  
143 **shown** in Fig. 3. Thanks to a negative lens, the whole beam shaping mask  
144 is illuminated by the generation laser. This mask consists of a series of  
145 transparent and opaque patterns (Fig. 2) printed on transparency films by  
146 a laser printer. Two identical masks are placed one after the other in the  
147 close vicinity of the plate in order to obtain a sufficient contrast. The normal  
148 surface displacement due to ultrasonic waves is detected on the other side of  
149 the sample by a two-wave mixing (TWM) interferometer (LU-TWM-ASGA,  
150 Tecnar Canada) whose bandwidth ranges from about 1 MHz to 40 MHz  
151 [23]. Note that the bandpass spectrum of the interferometer filter is smooth  
152 and still allows to detect displacement with frequency component down to  
153 about 300 kHz. The TWM is using a CW Nd:YAG laser, the beam of which  
154 is guided through an optical fiber to the TWM head including a neutral  
155 density filter and the focusing/collecting lens. The TWM head is mounted  
156 on a motorized linear stage so that the detection point is scannable over the  
157 sample. A second motorized linear stage can also be used to scan the sample  
158 in front of fixed generation pattern and detection point. Since generation  
159 and detection of elastic waves are on opposite sides, this setup is referred to  
160 as the transmission setup in the following.

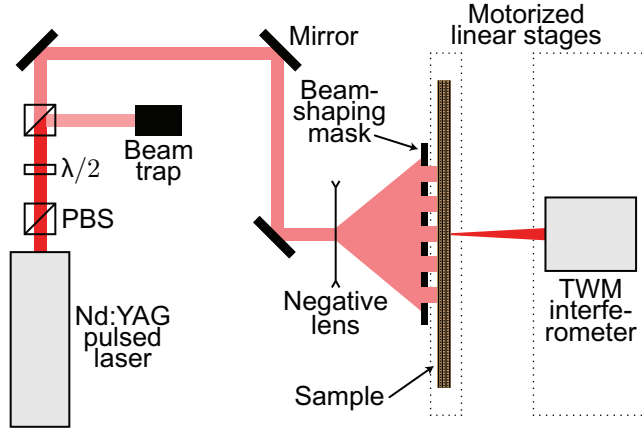


Figure 3: (color online) Schematics of the experimental transmission setup.

161 A second setup has been used in this study, with generation and detection  
 162 on the same side, which is referred to as the reflection setup in the following.  
 163 It is identical to the transmission setup, except that both generation laser  
 164 beam and TWM laser beam illuminate the same side of the sample, and  
 165 that the generation laser beam is frequency doubled in order not to dazzle  
 166 the TWM interferometer photodiode that is sensitive to 1064 nm radiation.  
 167 This setup can particularly be useful for a robot inspection and can give  
 168 additional information for a flaw characterization as it will be discussed in the  
 169 following: where the transmission setup detects a flaw without information  
 170 on its in-depth position, we will see that the reflection setup is able to give  
 171 information on the flaw position with respect to the depth.

172 Before applying the proposed method to the detection of a flaw in a  
 173 composite plate, it is first proposed to focus on the interest of using a beam-  
 174 shaping mask to enhance the ZGV Lamb modes in two samples: first, an  
 175 aluminum plate for trivial evidence, and then a composite plate.

176 **3. ZGV Lamb modes enhancement in aluminum and composite**  
177 **plates**

178 In order to validate preliminary results obtained with the transmission  
179 setup shown in Fig. 3, Fig. 4 presents the experimental results obtained in  
180 an 4.1 mm-thick aluminum plate using a single thermoelastic line source of  
181 dimensions 4.1 x 20 mm<sup>2</sup>. Figs. 4(a)-(b) are slightly saturated in order to  
182 improve readability.

183 The time domain B-scan [Fig. 4(a)] represents the normal surface dis-  
184 placement amplitude as a function of time and the TWM head position.  
185 The signals have been registered over 200  $\mu$ s with the TWM head position  
186 ranging from -50 mm to +50 mm with a 0.5 mm step. Two different kinds  
187 of modes are visible: (i) the propagating modes starting at the origin in time  
188 and space, and (ii) the ZGV Lamb modes that are visible in time after the  
189 propagating modes. The ZGV modes are evidenced by a succession of max-  
190 ima and minima in time and space, typical of the single frequency and the  
191 interferential nature of the ZGV modes.

192 The frequency domain B-scan [Fig. 4(b)] represents the spectral ampli-  
193 tude module of each A-scan constituting the time domain B-scan as a func-  
194 tion of the TWM head position. Each spectrum constituting the frequency  
195 domain B-scan has been calculated over the whole corresponding A-scan. At  
196 the first, i.e. lowest, expected ZGV Lamb mode frequency,  $f_{ZGV}^{Al} \approx 694$  kHz,  
197 there is a maxima and minima succession in space that is typical of ZGV  
198 Lamb modes obtained with a thermoelastic line source. When zooming at  
199 the ZGV frequency [Fig. 4(c)], the first ZGV peak amplitude as a func-  
200 tion of the TWM head position (solid) shows the expected theoretical shape

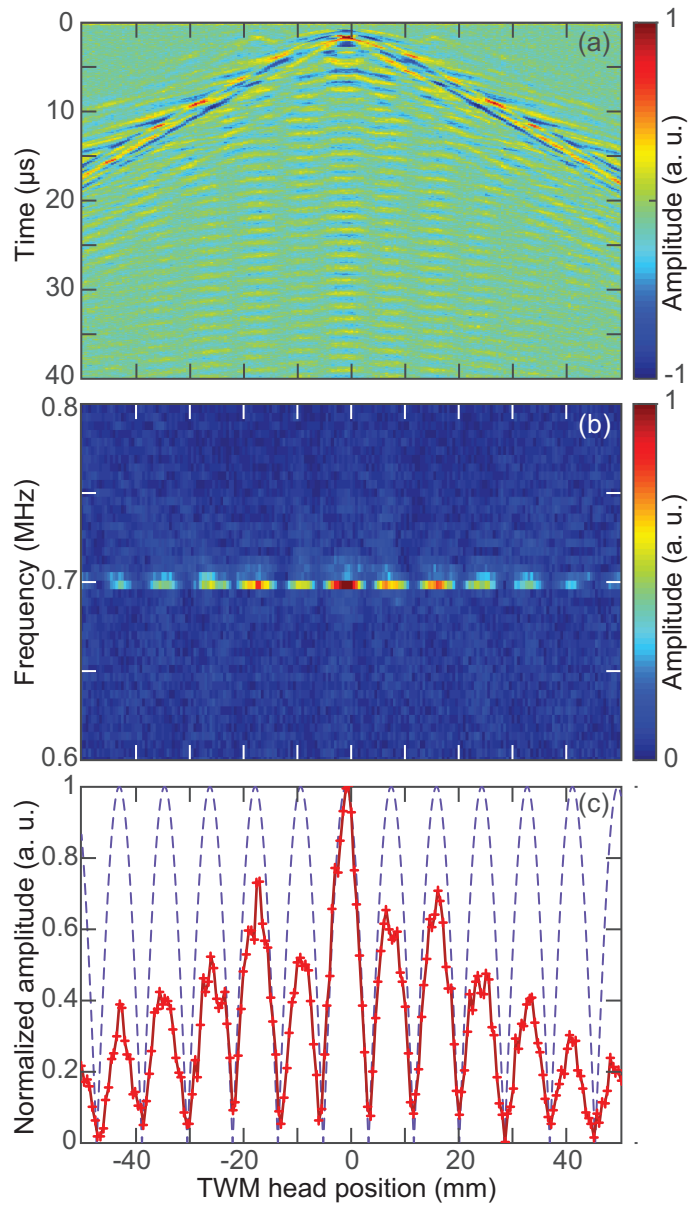


Figure 4: (color online) The thermoelastic source is a line  $4.1 \times 20 \text{ mm}^2$ : (a) time domain and (b) frequency domain B-scans as a function of the TWM head position. (c) First ZGV peak amplitude vs. TWM head position: experimental (solid) and theoretical (dashed) curves.

201 (dashed), especially regarding the minima. As expected theoretically, the  
 202 amplitude of the experimental curve decays with the distance from the line  
 203 source position because of the line source finite dimensions.

204 It is now proposed to compare this result obtained with a single line  
 205 source to the results obtained with a shaped source composed of lines spaced  
 206 by either  $\lambda_{ZGV}^{Al}$  or  $\lambda_{ZGV}^{Al}/2$ . Figure 5 presents the amplitude of the first ZGV  
 207 peak as a function of the TWM head position when the thermoelastic source  
 208 is made of: a single line (solid), multiple lines spaced by  $\lambda_{ZGV}^{Al}$  (dashed),  
 209 and multiple lines spaced by  $\lambda_{ZGV}^{Al}/2$  (dash-dotted). The Frobenius norm  
 210 (Euclidian norm) of each normal displacement field is used to normalize each  
 211 corresponding curve in Fig. 5, in order for the changes in the absorbed laser  
 212 power between the different cases to be compensated.

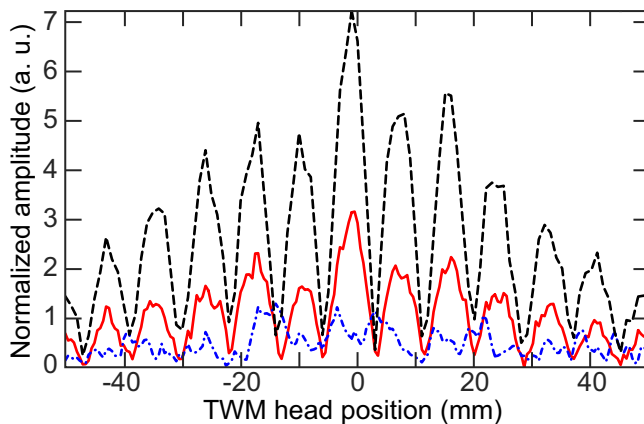


Figure 5: (color online) Normalized first ZGV peak amplitude vs. TWM head position when the thermoelastic source is a single line (solid), multiple lines spaced by  $\lambda_{ZGV}^{Al}$  (dashed) and multiple lines spaced by  $\lambda_{ZGV}^{Al}/2$  (dash-dotted).

213 When the lines are spaced by  $\lambda_{ZGV}^{Al}$ , the ZGV Lamb modes are enhanced:  
 214 they interfere constructively. On the contrary, when the lines are spaced

215 by  $\lambda_{ZGV}^{Al}/2$ , the ZGV Lamb mode amplitudes are reduced: they interfere  
 216 destructively. As expected, a mask consisting of slits spaced by the ZGV  
 217 wavelength enhances the ZGV Lamb modes generation in aluminum com-  
 218 pared to a mask consisting of a single slit. The interest of this beam-shaping  
 219 method being demonstrated in a metal plate, it is now examined in the more  
 220 challenging case of a composite plate.

221 The beam-shaping mask used with the composite plate consists of three  
 222 slits spaced by  $\lambda_{ZGV}^{comp}$ . Figures 6(a)-(c) show the experimental results. Fig-  
 223 ure 6(a) stands for the time domain B-scan, while Fig. 6(b) shows the fre-  
 224 quency domain B-scan. Figures 6(a)-(b) are slightly saturated in order to  
 225 improve readability. The amplitude of the first ZGV peak with respect to the  
 226 TWM head position obtained for the three-line source (thick line) is com-  
 227 pared to the same amplitude obtained with a single line source (thin line)  
 228 in Fig. 6(c). The ZGV peak amplitudes in Fig. 6(c) are normalized follow-  
 229 ing the same method as the one described for aluminum. **The comparison**  
 230 **between the thin and thick lines in Fig. 5(c) clearly demonstrates that the**  
 231 **ZGV peak is almost not observable when one slit is used. This emphasizes**  
 232 **that it is preferable to use three slits rather than one for the investigation of**  
 233 **a composite plate in order to increase the generation efficiency of the ZGV**  
 234 **mode and to get a sufficiently large signal to noise ratio for this particular**  
 235 **mode. Note that it is not the case for the Aluminum, where the ZGV mode**  
 236 **is well detectable when using one slit (cf. Fig. 4).**

237 The time domain B-scan [Fig. 6(a)] highlights the propagating modes  
 238 and we slightly see the ZGV Lamb modes. The frequency domain B-scan  
 239 [Fig. 6(b)] points out the ZGV Lamb modes at the frequency  $f_{ZGV}^{comp} \approx 0.480$  MHz,

240 which is confirmed by Fig. 6(c). Indeed, as ZGV peaks correspond to energy  
 241 peaks, they are expected to be spaced by half the ZGV wavelength, that  
 242 is to say that ZGV peaks are expected to be located in the middle of each  
 243 illuminated slits as well as centrally located between two adjacent slits. As  
 244 Fig. 6(c) shows these peaks on the slits location (under black arrows) and  
 245 centrally located between two adjacent slits (under gray arrows), this result  
 246 tends to prove the enhancement of the ZGV mode in the composite plate  
 247 thanks to the proposed beam-shaping mask.

248 In order to obtain Fig. 6(c), the ZGV peak amplitude was measured as the  
 249 maximum spectral amplitude module between 0.475 MHz and 0.485 MHz.  
 250 This frequency range can be related to a possible sample thickness variation  
 251 since the product of the ZGV mode frequency  $f_{ZGV}$  by the sample thickness is  
 252 constant. Hence, the average ZGV frequency  $(f_{ZGV})_0$  and the ZGV frequency  
 253 variation  $\Delta f_{ZGV}$  on the one hand, and the average sample thickness  $d_0$  and  
 254 the sample thickness variation  $\Delta d$  on the other hand, are related to each  
 255 other:

$$\frac{\Delta d}{d_0} = -\frac{\Delta f_{ZGV}}{(f_{ZGV})_0}. \quad (1)$$

257 The range [0.475-0.485] MHz leads to a thickness variation  $\Delta d$  of about  
 258  $\pm 33 \mu\text{m}$ . This sample thickness variation is very small and it is consistent  
 259 with the precision of the sample fabrication process.

260 As the beam-shaping method is validated to enhance ZGV Lamb modes  
 261 in the composite plate, a suitable mask with slits spaced by  $\lambda_{ZGV}$  is now  
 262 used for an NDT application.

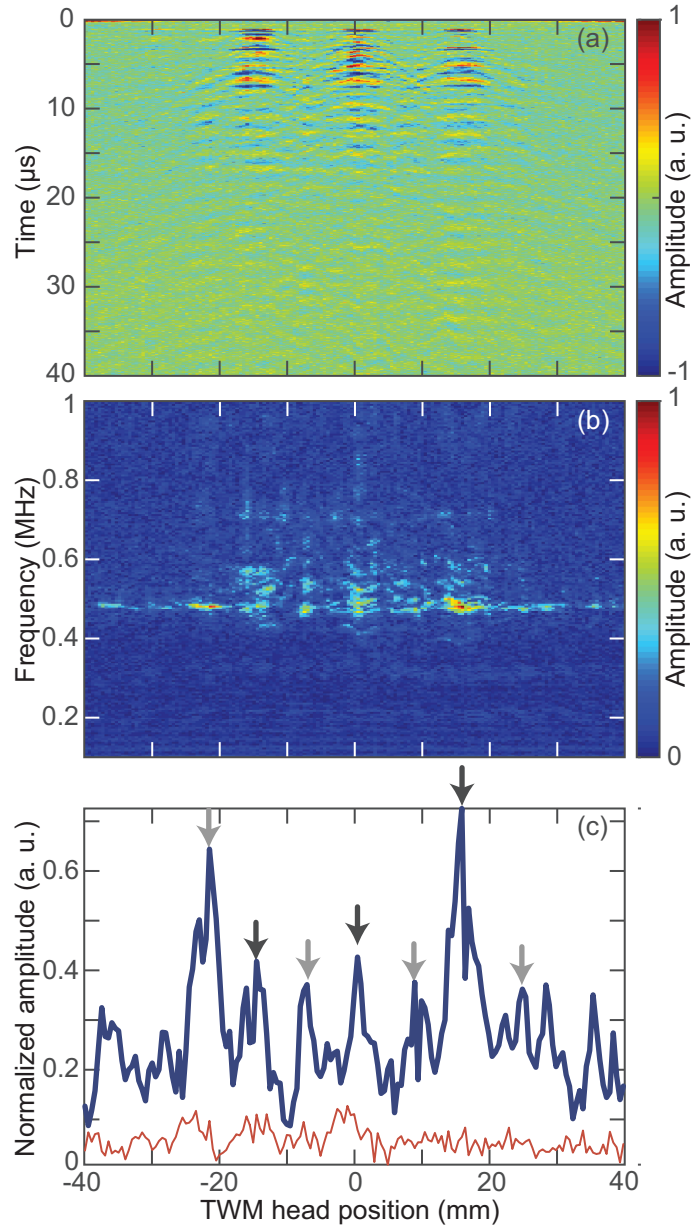


Figure 6: (color online) Results obtained in the composite plate with a thermoelastic source made of three lines: (a) time domain and (b) frequency domain B-scans vs. TWM head position. (c) Normalized amplitude of the first ZGV peak vs. TWM head position (thick line) compared with the result obtained with a single line source (thin line).

263 **4. NDT application in a composite plate**

264 The reflection setup described in Sec. 2 is now used to scan the composite  
265 plate in front of both spatially fixed Nd:YAG frequency doubled laser beam  
266 and TWM interferometer beam. The former is shaped by a mask having three  
267 slits spaced by  $\lambda_{ZGV}^{comp}$  and the latter being focused to a point in the middle  
268 of the beam shaping mask (middle line). As quickly explained in Sec. 2, the  
269 choice of using a reflection setup instead of the so-far used transmission setup  
270 is twofold: (i) this is closer to industrial applicability, and (ii) the flaw in the  
271 tested sample is such that, at the flaw location, there is no direct transmission  
272 of the elastic waves through the flaw, making the lateral detection of the flaw  
273 easy but not the in-depth location. We will see that using a reflection setup  
274 can lead to this in-depth characterization of the flaw.

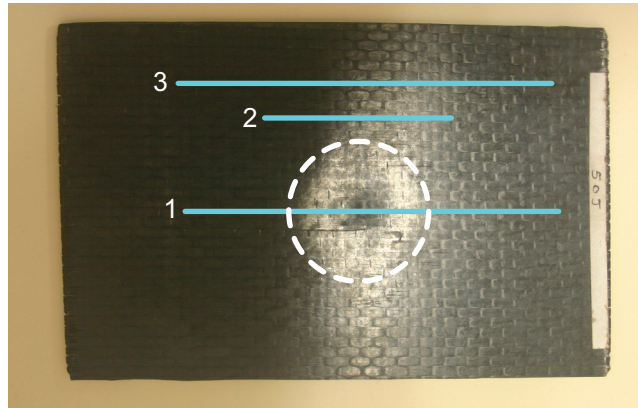


Figure 7: (color online) Composite sample and representation of the scan lines (solid). Dashed white line circle: maximum size of the flaw observed optically.

275 The composite sample presented in Fig. 7 has been impacted by a 50 J  
276 centered shock. The 50 J shock was obtained thanks to the drop of a hemi-  
277 spherical mass with a diameter of 25 mm. The sample was clamped on a

278 bearing having a 40 mm-diameter hole, centered with respect to the drop  
 279 mass axis. The first scan line (line 1) crosses the impact whereas the second  
 280 scan line (line 2) is near the impact location and the third scan line (line  
 281 3) is far from the impact location. Within all these scans, the line sources  
 282 composing the shaped thermoelastic source were perpendicular to the scan  
 283 direction. Regarding line 3, note that the shaped thermoelastic source is at  
 284 least 5 mm away from both the plate edge and the impact location, whatever  
 285 the plate position during the scan is.

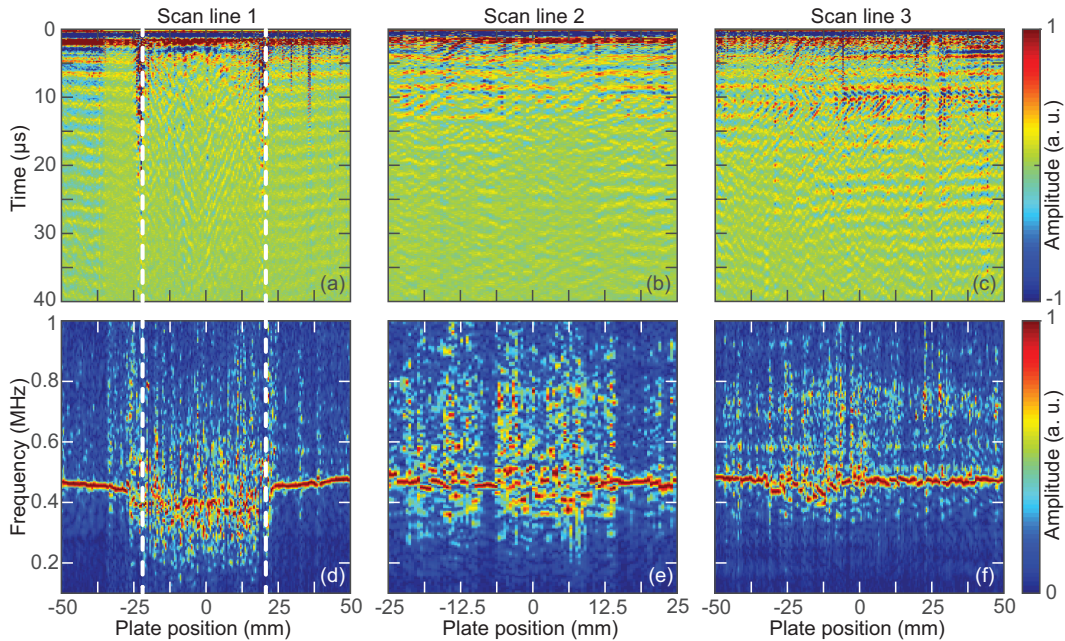


Figure 8: (color online) Time domain B-scans of the composite plate when the scan line is: line 1 across the impact location (a), line 2 near the impact location (b), and line 3 far from the impact location (c). The related frequency domain B-scans obtained with a Hann time window (respectively d, e and f). Dashed white lines: maximum dimension of the flaw observed optically.

286 The time domain B-scan signals have been registered over 200  $\mu\text{s}$  with

287 the plate position ranging from  $-50$  mm to  $+50$  mm [Fig. 8(a) and Fig. 8(c)]  
288 or from  $-25$  mm to  $+25$  mm [Fig. 8(b)] with a  $0.5$  mm step. Each A-scan for  
289 a given plate position is numerically post-processed in order to have a zero  
290 mean value over the useful signal duration, i.e. from  $10$   $\mu$ s to  $100$   $\mu$ s. The  
291 frequency domain B-scans have then been calculated over the whole time  
292 domain signals filtered by a Hann time window ranging from  $0$   $\mu$ s to  $100$   $\mu$ s  
293 in order to emphasize the ZGV Lamb modes. The spectrum amplitude for a  
294 given plate position is normalized to its maximum.

295 In Fig. 8(a), the time domain B-scan across the impact location high-  
296 lights the impact edges marked by the dashed white lines (cf. also Fig. 7).  
297 Moreover, regular successions of maxima and minima in time, representative  
298 of ZGV oscillations, can be observed outside of the impact location (in a  
299 healthy zone) whereas the signal appears disturbed inside the impact loca-  
300 tion. The time domain B-scans near the impact location and far from the  
301 impact location [Fig. 8(b) and Fig. 8(c), respectively] show minor changes  
302 with the plate position and no flaw is clearly evidenced.

303 The frequency domain B-scan across the impact location [Fig. 8(d)] also  
304 clearly highlights the impact as only the ZGV frequency is visible outside  
305 the impact location whereas on the impact location the dominant frequency  
306 components are spread out over the range  $\sim 200 - 800$  kHz and show quick  
307 variations in space. Let us also notice that the ZGV frequency decreases  
308 almost linearly when the signal measurement gets closer to the impact. As  
309 the product  $f_{ZGV}$  by the thickness is constant, this shows that either the  
310 plate thickness increases with the impact vicinity (the 50 J impact has lead  
311 to a bulge at the vicinity of the impact) or the elastic moduli diminish.

312 The frequency domain B-scan near the impact location [Fig. 8(e)] also shows  
313 changing multiple frequency components between  $-5$  mm and  $+15$  mm that  
314 could be due to the impact vicinity. Moreover, farther from the impact  
315 location, i.e. between  $-25$  mm and  $-10$  mm, multiple frequency components  
316 also appear whereas this zone should be healthy. The frequency domain B-  
317 scan far from the impact location [Fig. 8(f)] shows that the main frequency  
318 component is the ZGV frequency below  $-30$  mm and above  $0$  mm; these zones  
319 can thus be considered as quasi-healthy zones. On the contrary, between  
320  $-30$  mm and  $0$  mm, a hidden flaw is detected. This confirms the previous  
321 result [Fig. 8(e)] highlighting a flaw on a zone that should be healthy.

322 These results have been compared to the composite plate inspection ob-  
323 tained with a system called LUCIE, the technical specifications of which are  
324 gathered in Ref. [24]. Note that the minimum laser fluence delivered by the  
325 pump laser ( $\text{CO}_2$ ,  $270$  mJ,  $100$  ns) in the LUCIE system is  $1.5 \text{ MW}\cdot\text{cm}^{-2}$ ,  
326 which is below the damage threshold of the composite. **Signals are gathered**  
327 **at a fast rate by the LUCIE system thanks to its scan head which includes**  
328 **both the pump laser and the probe laser used for the interferometric mea-**  
329 **surement of the sample surface velocity. Figure 9 represents the C-scan**  
330 **inspection of the composite plate consisting in measuring the ratio of two**  
331 **ultrasonic echo amplitudes as a function of the position on the plate: the ra-**  
332 **tio of the amplitudes of the second ultrasonic echo detected (acoustic waves**  
333 **reflected by the rear surface of the plate or by a defect) to the first ultrasonic**  
334 **echo detected (corresponding to the surface expansion due to laser absorp-**  
335 **tion). Note that the ratio can be done after filtering the collected raw data**  
336 with a selective band-pass filter. LUCIE's data post-processing may also give

337 an image (not shown in this paper) of the time of flight difference between  
 338 the first and the second detected acoustic echo, although this image is not  
 339 precise for in-depth localization of defects close to the surface. The presented  
 340 scan (Fig. 9) shows two major results. First, the 50 J impact is very well  
 341 identified by the centered zone that shows the lowest value. Second, on the  
 342 healthy zone scanned previously (cf. line 3 in Fig. 7), the ratio has either  
 343 values in  $[4.55-9.75]$  % that should be indicative of a real healthy zone or  
 344 weak values lower than 3.25 % that are indicative of a flaw. This last result  
 345 confirms the presence of the hidden flaw detected previously along the scan  
 346 line 3 by the method proposed by the authors.

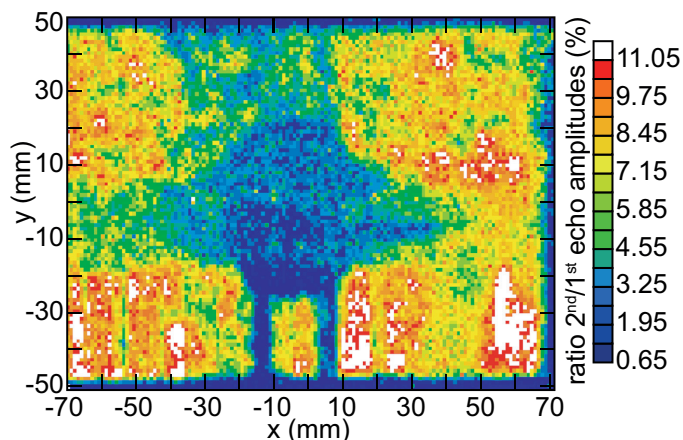


Figure 9: (color online) C-scan inspection of the composite plate obtained with the LUCIE system: ratio of the second ultrasonic echo amplitude to the first ultrasonic echo amplitude

347 Using the experimental transmission setup, a supplementary scan has  
 348 been done along the scan line 1, the results of which are not presented in  
 349 this paper. The observation is that, at the flaw location, no elastic wave is  
 350 directly transmitted. This observation probably means that the 50 J impact

351 produced a delamination inside the composite plate.

352 Let us consider that the impact produced a delamination inside the com-  
353 posite plate, hence splitting the plate into a minimum of two thinner plates  
354 one above the other. If we assume that laser generated ultrasonic waves  
355 interact only with the top plate, several mechanisms can explain why the  
356 frequency domain B-scans show multiple frequency components on the de-  
357 lamination location. A given frequency component different from the ZGV  
358 mode frequency of the plate can be due to a membrane resonance effect [25]  
359 or to a local defect resonance [26]. It could even be due to another ZGV mode  
360 frequency associated to a smaller thickness than the one of the plate. A flaw  
361 resonance frequency  $f_r$  can be estimated by assuming a circular clamped  
362 membrane:

$$363 \quad f_r = \frac{1.88h}{d^2} \sqrt{\frac{E}{\rho(1-\nu^2)}}, \quad (2)$$

364 where  $h$  and  $d$  are the flaw depth and diameter respectively, and  $E$ ,  $\rho$  and  $\nu$   
365 are the sample Young's modulus, density and Poisson ratio respectively.

366 Assuming that the characteristic frequency is due to a circular flaw res-  
367 onance and using the following material parameters:  $h = 300 \mu\text{m}$  (a ply  
368 thickness),  $E = 15 \text{ GPa}$ ,  $\rho = 1540 \text{ kg/m}^3$ , and  $\nu = 0.2$ , the flaw dimension  
369 could be estimated as  $d = 2.1 \text{ mm}$ , the flaw resonance being in that case  
370  $f_r \simeq 0.41 \text{ MHz}$ . This estimates is in good agreement with the frequency val-  
371 ues observed in the frequency domain B-scans in Fig. 8. More information on  
372 the material parameters and possible flaw geometry is necessary. We believe  
373 however that in the near future the development of a realistic model could  
374 lead to quantitative estimates of defect parameters relevant for the structural  
375 health assessment of composite structures.

## 376 **5. Conclusion**

377 We have presented a method enabling ZGV Lamb modes enhancement  
378 thanks to the beam shaping of the generation laser, making use of a mask  
379 with slits spaced by the ZGV wavelength. First, ZGV Lamb modes have  
380 been analyzed in an aluminum plate to validate the possibility to enhance  
381 or reduce their amplitude depending on the thermoelastic line sources spac-  
382 ing. It has been shown that ZGV Lamb modes interfere constructively when  
383 the line sources spacing equals the ZGV wavelength whereas they interfere  
384 destructively when the spacing is halved.

385 After the thorough characterization of a composite plate that resulted  
386 in the ZGV wavelength determination, the beam-shaping method has been  
387 applied to the composite sample. Experimental results demonstrate a ZGV  
388 Lamb mode enhancement, hence validating the beam-shaping method also  
389 in the case of a composite sample. Finally, by scanning over the sample,  
390 the measured signal frequency content near the ZGV frequency has proven  
391 its ability to distinguish between healthy zones and an impacted zone of a  
392 composite plate, and also to detect flaw zones that are not visually detectable.  
393 The next step could possibly be to extract quantitative information from the  
394 dominant frequencies of the B-scans compared to those predicted by the  
395 mechanical models of the defects.

## 396 **6. Acknowledgments**

397 This presentation is part of the LUCITA project managed by IRT Jules  
398 Verne (French Institute in Research and Technology in Advanced Manu-  
399 facturing Technologies for Composite, Metallic and Hybrid Structures). The

400 authors wish to associate the industrial and academic partners of this project:  
401 Airbus Group Innovations and STELIA Aerospace; EMN-Subatech and LAUM  
402 respectively.

### 403 **References**

- 404 [1] J. Cooper, R. A. Crosbie, R. J. Dewhurst, A. D. W. McKie, and S. B.  
405 Palmer, Surface acoustic wave interactions with cracks and slots: A  
406 noncontacting study using lasers, *IEEE Trans. Ultrason. Ferroelectr.*  
407 *Freq. Control.* **33**, 462–470 (1986).
- 408 [2] D. W. Schindel, D. A. Hutchins, S. T. Smith, and B. Farahbakhsh,  
409 Hightemperature pulsed photoacoustic studies of surface waves on solids,  
410 *J. Acoust. Soc. Am.* **95**, 2517–2524 (1994).
- 411 [3] N. Guo and P. Cawley, The interaction of Lamb waves with delamina-  
412 tions in composite laminates, *J. Acoust. Soc. Am.* **94**, 2240–2246 (1993).
- 413 [4] A. Blouin, C. Néron, B. Campagne, and J.-P. Monchalain, Applications  
414 of laser-ultrasonics and laser-tapping to aerospace composite structures.,  
415 in *Conference proceedings of 17th WCNDT. Shanghai.*, page 7 (2008).
- 416 [5] P. A. Fomitchov, A. K. Kromin, S. Krishnaswamy, and J. D. Achenbach,  
417 Imaging of damage in sandwich composite structures using a scanning  
418 laser source technique, *Compos. Part B-Eng.* **35**, 557–562 (2004), marine  
419 Composites.
- 420 [6] A. A. Karabutov and N. B. Podymova, Quantitative analysis of the  
421 influence of voids and delaminations on acoustic attenuation in CFRP

- 422 composites by the laser-ultrasonic spectroscopy method, *Compos. Part*  
423 *B-Eng.* **56**, 238–244 (2014).
- 424 [7] M. Spies and W. Jager, Synthetic aperture focusing for defect recon-  
425 struction in anisotropic media, *Ultrasonics* **41**, 125–131 (2003).
- 426 [8] S. Rodriguez, M. Castaings, M. Deschamps, and E. Ducasse, Topological  
427 imaging of defects in anisotropic plates, in V. Le Cam, L. Mevel, and  
428 F. Schoefs, editors, *EWSHM - 7th European Workshop on Structural*  
429 *Health Monitoring*, pages 1155–1162 (2014).
- 430 [9] D. Clorenec, C. Prada, and D. Royer, Local and noncontact measure-  
431 ments of bulk acoustic wave velocities in thin isotropic plates and shells  
432 using zero group velocity Lamb modes, *J. Appl. Phys.* **101**, 034908  
433 (2007).
- 434 [10] D. Clorenec, C. Prada, and D. Royer, Laser ultrasonic inspection of  
435 plates using zero-group velocity Lamb modes, *IEEE Trans. Ultrason.*  
436 *Ferroelectr. Freq. Control.* **57**, 1125–1132 (2010).
- 437 [11] J. F. Ready, in J. F. Ready, editor, *Effects of High-Power Laser Radia-*  
438 *tion*, chapter 3, pages 67–125, Academic Press (1971).
- 439 [12] O. Balogun, T. W. Murray, and C. Prada, Simulation and measure-  
440 ment of the optical excitation of the  $S_1$  zero group velocity Lamb wave  
441 resonance in plates, *J. Appl. Phys.* **102**, 064914 (2007).
- 442 [13] J. A. Rogers and K. A. Nelson, Study of lamb acoustic waveguide modes  
443 in unsupported polyimide thin films using real-time impulsive stimulated  
444 thermal scattering, *J. Appl. Phys.* **75**, 1534–1556 (1994).

- 445 [14] J. A. Rogers, A. A. Maznev, M. J. Banet, and K. A. Nelson, Optical  
446 generation and characterization of acoustic waves in thin films: funda-  
447 mentals and applications, *Annu. Rev. Mater. Sci.* **30**, 117–157 (2000).
- 448 [15] A. A. Maznev and A. G. Every, Surface acoustic waves with negative  
449 group velocity in a thin film structure on silicon, *Appl. Phys. Lett.* **95**,  
450 011903 (2009).
- 451 [16] A. Bennis, A. M. Lomonosov, Z. H. Shen, and P. Hess, Laser-based mea-  
452 surement of elastic and mechanical properties of layered polycrystalline  
453 silicon structures with projection masks, *Appl. Phys. Lett.* **88**, 101915  
454 (2006).
- 455 [17] C. Grünsteidl, I. A. Veres, J. Roither, P. Burgholzer, T. W. Murray, and  
456 T. Berer, Spatial and temporal frequency domain laser-ultrasound ap-  
457 plied in the direct measurement of dispersion relations of surface acoustic  
458 waves, *Appl. Phys. Lett.* **102**, 011103 (2013).
- 459 [18] F. Reverdy and B. Audoin, Elastic constants determination of  
460 anisotropic materials from phase velocities of acoustic waves generated  
461 and detected by lasers, *J. Acoust. Soc. Am.* **109**, 1965–1972 (2001).
- 462 [19] B. Hosten and B. Castagnede, Optimisation du calcul des constantes  
463 élastiques à partir des mesures de vitesses d’une onde ultrasonore, *C. R.*  
464 *Acad. Sc. Paris*, **296**, 297–300 (1983).
- 465 [20] A. L. Shuvalov and O. Poncelet, On the backward lamb waves near  
466 thickness resonances in anisotropic plates, *Int. J. Sol. Struct.* **45**, 3430–  
467 3448 (2008).

- 468 [21] T. Hussain and F. Ahmad, Lamb modes with multiple zero-group ve-  
469        velocity points in an orthotropic plate, *J. Acoust. Soc. Am.* **132**, 641–645  
470        (2012).
- 471 [22] S. Raetz, J. Laurent, T. Dehoux, D. Royer, B. Audoin, and C. Prada,  
472        Effect of refracted light distribution on the photoelastic generation of  
473        zero-group velocity Lamb modes in optically low-absorbing plates, *J.*  
474        *Acoust. Soc. Am.* **138**, 3522–3530 (2015).
- 475 [23] R. K. Ing and J. Monchalín, Broadband optical detection of ultrasound  
476        by two-wave mixing in a photorefractive crystal, *Appl. Phys. Lett.* **59**,  
477        3233–3235 (1991).
- 478 [24] B. Campagne, H. Voillaume, L. Gouzerh, and F. Bentouhami, Laser ul-  
479        trasonic developments for NDT of aeronautic composite parts, in *13th*  
480        *International Symposium on Nondestructive Characterization of Mate-*  
481        *rials (NDCM-XIII) 2013, Le Mans, France*, volume 19, NDT.net, The  
482        e-Journal of Nondestructive Testing & Ultrasonics (2014).
- 483 [25] P. Cawley and C. Theodorakopoulos, The membrane resonance method  
484        of non-destructive testing, *J. Sound Vibrat.* **130**, 299–311 (1989).
- 485 [26] I. Solodov, J. Bai, S. Bekgulyan, and G. Busse, A local defect resonance  
486        to enhance acoustic wave-defect interaction in ultrasonic nondestructive  
487        evaluation, *Appl. Phys. Lett.* **99**, 211911 (2011).

488 **List of Figures**

489 1 (color online) Dispersion curves of the symmetric (solid line)  
490 and antisymmetric (dashed line) Lamb modes calculated in a  
491 3.2-mm-thick composite plate. The first ZGV mode is shown  
492 by the vertical arrow and has a wavelength of  $\lambda_{ZGV}^{comp} \approx 15.3$  mm. 6  
493 2 (color online) Illustration of the ZGV Lamb mode generation  
494 using a beam-shaping mask. The generation laser beam is  
495 shaped with periodic slits whose spacing matches the ZGV  
496 wavelength. . . . . 7  
497 3 (color online) Schematics of the experimental transmission setup. 9  
498 4 (color online) The thermoelastic source is a line 4.1 x 20 mm<sup>2</sup>:  
499 (a) time domain and (b) frequency domain B-scans as a func-  
500 tion of the TWM head position. (c) First ZGV peak amplitude  
501 vs. TWM head position: experimental (solid) and theoretical  
502 (dashed) curves. . . . . 11  
503 5 (color online) Normalized first ZGV peak amplitude vs. TWM  
504 head position when the thermoelastic source is a single line  
505 (solid), multiple lines spaced by  $\lambda_{ZGV}^{Al}$  (dashed) and multiple  
506 lines spaced by  $\lambda_{ZGV}^{Al}/2$  (dash-dotted). . . . . 12  
507 6 (color online) Results obtained in the composite plate with a  
508 thermoelastic source made of three lines: (a) time domain and  
509 (b) frequency domain B-scans vs. TWM head position. (c)  
510 Normalized amplitude of the first ZGV peak vs. TWM head  
511 position (thick line) compared with the result obtained with  
512 a single line source (thin line). . . . . 15

513	7	(color online) Composite sample and representation of the scan	
514		lines (solid). Dashed white line circle: maximum size of the	
515		flaw observed optically. . . . .	16
516	8	(color online) Time domain B-scans of the composite plate	
517		when the scan line is: line 1 across the impact location (a),	
518		line 2 near the impact location (b), and line 3 far from the	
519		impact location (c). The related frequency domain B-scans	
520		obtained with a Hann time window (respectively d, e and f).	
521		Dashed white lines: maximum dimension of the flaw observed	
522		optically. . . . .	17
523	9	(color online) C-scan inspection of the composite plate ob-	
524		tained with the LUCIE system: ratio of the second ultrasonic	
525		echo amplitude to the first ultrasonic echo amplitude . . . . .	20